STUDIES OF THE SHADOWING OF TeV COSMIC RAYS BY THE MOON AND THE SUN

M. O. Wascko,[1,a] R. Atkins,[2] W. Benbow,[3] D. Berley,[4] M.-L. Chen,[4,b] D. G. Coyne,[3] B. L. Dingus,[2] D. E. Dorfan,[3] R. W. Ellsworth,[5] A. Falcone,[6] L. Fleysher,[7] R. Fleysher,[7] G. Gisler,[8] J. A. Goodman,[4] T. J. Haines,[8] C. M. Hoffman*,[8] S. Hugenberger,[9] L. A. Kelley,[3] I. Leonor,[9] M. McConnell,[6] J. F. McCullough,[3] J. E. McEnery,[2] R. S. Miller,[6] A. I. Mincer,[7] M. F. Morales,[3] P. Nemethy,[7] J. M. Ryan,[6] F. Samuelson,[8] B. Shen,[1] A. Shoup,[9] G. Sinnis,[8] A. J. Smith,[4] G. W. Sullivan,[4] O. T. Tumer,[1] K. Wang,[1,d] S. Westerhoff,[3,c] D. A. Williams,[3] T. Yang,[3] G. B. Yodh[9]
(The Milagro Collaboration)

[1]University of California, Riverside, CA 92521
[2]University of Wisconsin, Madison, WI 53706
[3]University of California, Santa Cruz, CA 95064
[4]University of Maryland, College Park, MD 20742
[5]George Mason University, Fairfax, VA22030
[6]University of New Hampshire, Durham, NH 03824-3525
[7]New York University, New York, NY 10003
[8]Los Alamos National Laboratory, Los Alamos, NM 87545
[9]University of California, Irvine, CA 92717

[a]Now at Louisiana State University, Baton Rouge, LA 70803
[b]Now at Brookhaven National Laboratory, Upton, NY 11973
[c]Now at Columbia University, New York, NY 10027
[d]Now at Armillaire Technologies Inc., Bethesda, MD 20817

Abstract

The shadowing of TeV cosmic rays by the moon and by the sun have been observed with data from the Milagrito air-shower-particle detector. The significance of the observed shadows are each ~10σ. These data are used to study the systematic pointing accuracy and angular resolution of Milagrito. The shadow of the moon is clearly displaced by the geomagnetic field, which provides an estimate of the energy response of Milagrito, and allows a search for cosmic antiprotons. The 95% confidence level upper limit for the ratio $\bar{p}/p$ in ~3 TeV cosmic rays is 17%. The observed position of the shadow of the sun contains information on the solar magnetic field.

* Corresponding author: Cyrus Hoffman MS H803 Los Alamos National Laboratory, Los Alamos, NM 87544 USA   Tel.: +1 505 667 5876; e-mail: cy@lanl.gov.

1. Introduction

Clark first proposed in 1957 that the shadow of the moon and the sun could be observed with high-energy cosmic rays,[1] noting that this might be a useful way to gain new information about the magnetic fields of these bodies. The idea lay dormant until 1985 when the prospect of new air-shower arrays with large collection areas and good angular resolution prompted Lloyd-Evans [2] and Linsley [3] to consider studying the shadows. Lloyd-Evans suggested using the lunar shadow to calibrate the detector directional resolution, and considered the possibility of using the displacement of shadow of the sun by the solar magnetic field to measure the average mass composition for high-energy cosmic rays. In addition to considering these topics, Linsley suggested looking for a solar shadow magnetically displaced in the opposite direction to search for high-energy antiprotons.

It wasn't until 1991 that an extensive air shower (EAS) array had good enough angular resolution and a large enough data set to observe the shadows of the sun and moon with high-energy cosmic rays.[4] Since that time, a number of other air-shower experiments have used the measured shadow of the sun and moon to check the detector angular resolution and pointing.[5-8] The high-altitude Tibet array [5] observed a clear deflection and possible distortion of the solar shadow in 1990-1 with ~10-TeV cosmic rays, and possibly a small deflection of the lunar shadow. More extensive data, covering the period from 1990-1997, shows that the solar shadow appears to move in correlation with the large-scale structure of the solar and interplanetary magnetic fields, and that the observed lunar shadow is offset ~$0.2° \pm 0.15°$ by the geomagnetic field.[9]

Urban and collaborators [10] explored the possibility of observing air showers coming from directions near the moon with an air Cerenkov telescope to search for cosmic antiprotons. However, attempts to use the Whipple 10-m telescope with filters to suppress unwanted moonlight have not demonstrated the needed sensitivity.[11] Chantell *et al.* [12] analyzed the moon shadow observed by the Tibet array and derived an upper limit on the $\bar{p}/p$ ratio of 43% (no confidence level given) for energies ~10 TeV.

We report here on observations of the lunar and solar shadows with the Milagrito air-shower detector. These observations are used to study systematic pointing errors and the angular resolution of Milagrito, to establish the first direct check of the energy scale for a ground-based cosmic-ray detector, to establish an improved upper limit on the existence of cosmic antiprotons in the 1-TeV region, and to obtain information on the solar and interplanetary magnetic fields.

The Milagrito air-shower detector was sensitive to cosmic rays in the 1-TeV region. Milagrito used a 19×12 array of 20-cm-diameter photomultiplier tubes (PMTs) covering an area of 30 m $\times$ 50 m under ~1.5 m of water to detect the Cherenkov radiation produced in the water by EAS particles reaching the ground. Milagrito was located in the Jemez Mountains of New Mexico at an altitude of 2650 m above sea level, and operated from February 1997 to May 1998. The direction of the incident particle producing the EAS was reconstructed from the relative times at which the individual PMTs were struck by light produced by particles in the shower front. Details of the operation and performance of Milagrito is given in Atkins et al. (2000). [13]

2. Simulations
2.1 Simulation of the Moon Shadow

The response of Milagrito to cosmic rays was simulated in two steps. The first step, the cascade in the atmosphere from the first interaction down to the surface of the water in Milagrito, used the CORSIKA (version 5.61) simulation package. [14] The incident cosmic rays were assumed to be isotropic and to consist of a sum of protons, helium and CNO primaries, with fluxes and energy spectra taken from Refs. [15, 16]. The second step, the interaction of these particles in the water including the production and propagation of Cherenkov photons and the response of the PMTs to these photons, used the GEANT package. [17] GEANT can generate and track Cherenkov photons with the correct spectrum so that the wavelength dependence of light absorption, refraction, and transmission, and the quantum efficiency of the PMTs can be explicitly taken into account. The output of the simulation was an array of pulse heights and times for all of the PMTs. The simulated events were reconstructed with the same programs used to reconstruct data events.

2.2 Cosmic ray Deflection in the Geomagnetic Field

Charged cosmic rays are deflected by the geomagnetic field between the moon and the earth. This deflection ends in the upper atmosphere when the EAS, which is essentially electrically neutral, forms. The deflection causes the apparent shadow of the moon, reconstructed with the incident directions of the EAS, to be offset from the true position of the moon. A full understanding of the expected shape and location of the moon shadow requires a calculation of the deflection of cosmic rays in the geomagnetic field. The geomagnetic deflection was obtained by stepping oppositely-charged cosmic rays upwards from the top of the atmosphere above the location of Milagro through the geomagnetic field towards the position of the moon. The cosmic ray paths are bent by the geomagnetic field and arrive at a deflected position of the moon. Thus a cosmic ray coming from the actual direction of the moon will be deflected and appear on earth to come from a deflected apparent position of the moon.

The calculation used a Cartesian coordinate system with the origin at the center of the earth: this origin was used because the distance between the moon and the center of the earth is nearly constant over time. A simple dipole field with the dipole pointed toward the south magnetic pole was used. Comparisons with the World Magnetic Model WMM-2000 [18] showed negligible differences in cosmic ray deflections for zenith angles less than 45°. A look-up table of deflection values was constructed for all positions of the moon in the local sky (in steps of 1°) and several values of magnetic rigidity between 100 GV/c and 500 GV/c: Above 500 GV/c, the deflection is found to be inversely proportional to the rigidity so an extrapolation can be used.

The deflections depend on the location of the detector and the position of the moon in the sky. At Milagrito (106.68° W longitude, 35.88° N latitude) the cosmic ray shadow appears to be offset to the west and south (north) directions when the moon is rising (setting). Thus cosmic rays with a fixed magnetic rigidity produce a shadow for a full transit of the moon that is offset to the west and slightly broadened in the north-south direction: the size of the westward offset depends on the apparent declination of the moon, which varies over the lunar month. Cosmic rays with a spectrum of rigidities will produce a shadow with a low-rigidity tail towards the west.

2.3 Angular Resolution and Pointing

Previous analyses of Milagrito data [19] involved studies of point-source gamma-ray emission. The study described here involves extensive air showers produced by the isotropic flux of charged cosmic rays. Simulations indicate that the angular resolution is slightly worse for cosmic-ray

events than for gamma-ray events, and improves rapidly as the number of PMTs participating in the fit increases.[13]

The simulations also indicate that Milagrito had a systematic pointing error due to Cherenkov light traveling nearly horizontally in the water. Because the Cherenkov angle in water is 41°, relativistic charged particles with zenith angles >45° can produce Cherenkov light traveling nearly horizontally in the water, which can traverse large distances before striking a PMT. This will result in PMT pulses that are late relative to the shower front. This "late light" will tend to systematically cause the shower plane to be reconstructed with a zenith angle that is larger than the true zenith angle. This systematic error is more pronounced for showers with large zenith angles, although it is present even for relatively small zenith-angle showers due to the multiple scattering of shower particles. The systematic error also increases as the number of PMTs hit in an event decreases. Because the electronics registered the time of arrival of the first photoelectron in each PMT, the systematic error can be diminished by excluding PMTs with less than 2 photoelectrons from the event fit.

The parameters ζ_x and ζ_y were used in the study of the systematic pointing error to avoid the artificial singularity in spherical coordinates at $\theta = 0°$. ζ_x and ζ_y are defined in terms of the zenith angle (θ) and azimuthal angle (ϕ) via:

$$\sin(\zeta_x) = \sin\theta \cos\phi, \text{ and } \sin(\zeta_y) = \sin\theta \sin\phi. \tag{1}$$

2.4 Simulation Results

The systematic pointing error has been studied by comparing the input values of ζ_x and ζ_y with the values of these quantities from the fit to the simulated data. The values of $\Delta\zeta_x = \zeta_x^{Thrown} - \zeta_x^{Fit}$ were found for each simulated event and fit to a straight line as a function of ζ_x^{Thrown} and of ζ_x^{Fit} (and similarly for ζ_y). These fits yield the systematic error as a function of the true incident angle, and the reconstructed angle, respectively. The former is the actual systematic error: the latter can be used to correct the systematic error event-by-event. Figure 1 shows the dependence of the systematic error on N_{Fit}, the number of PMTs participating in the fit to the shower direction: the effect is largest for events with small values of N_{Fit}, as expected. It is important to note that the systematic pointing error should result in the moon shadow appearing too far south and smeared somewhat in the east-west direction, after averaging over a full transit of the moon.

Figure 2 shows two-dimensional plots of the simulated shadow of the moon from reconstructed events that would be blocked by the moon, before and after correcting for the systematic pointing error. Note that the southward displacement of the uncorrected shadow is removed by the correction, and that the corrected shadow is less smeared. In addition, the corrected shadow is displaced ~0.5° to the west by the geomagnetic field, and there is a hint of a low rigidity tail farther to the west. These effects are more easily seen in Figure 3, which shows projections of the shadow on the right ascension (α) and declination (δ) axes. Note that the uncorrected distributions are ~10% wider than the corrected distributions, and that the correction centers the shadow in δ. The asymmetry in the α distribution illustrates the effect of the geomagnetic field on low rigidity events.

Figure 4 shows the projection onto the α axis for the uncorrected moon shadow for proton, helium, and nitrogen primaries separately. The energy spectra and number of helium and nitrogen primaries thrown reproduce the measured [15,16] cosmic-ray fluxes for light and medium-weight nuclei. This shows that most of the shadow and virtually all of its geomagnetic offset are due to primary protons. Table 1 summarizes the results for the different species. It is perhaps surprising that the geomagnetic deflection is greater for proton events than for heavier primaries. While the heavier primaries have larger charges, the effective area of Milagrito falls off much more steeply at low energies for them than for protons [13] so that events with lower rigidity, which are most strongly deflected, are overwhelmingly due to protons.

Species	Spectral Index	Fraction of Events	Median Rigidity	Most Probable Deflection
Protons	-2.80	68%	2.4 TV/c	-0.26°
Helium	-2.64	28%	10.0 TV/c	-0.09°
Nitrogen	-2.67	4%	15.1 TV/c	-0.25°
All		100%	2.7 TV/c	-0.23°

Table 1: Expected properties of the moon shadow for different cosmic-ray species.

Figure 5 shows projections onto the α axis of the simulated shadow for different regions of N_{Fit}. The most probable deflection grows as N_{Fit} decreases, indicating that the typical rigidity of events with large N_{Fit} is higher.

All of these studies have involved simulated events coming from the direction of the moon in the absence of background. While this is a convenient way to study the expected properties of the shadow, a true comparison with data requires background events and treating the moon as a sink rather than a source of events. The background for the simulation is obtained from the data in the same manner that it is obtained in the analysis of the data itself, as discussed below. The normalization of the depth of the simulated shadow is fixed by the density of background events in the vicinity of the moon and the fact that the moon appears in the sky to be a circle with a 0.26° radius.

3. Data Analysis
3.1 Sky Map
The events were reconstructed as described in Reference 19. Events with $N_{Fit} > 30$ and zenith angles $< 45°$ were put into a sky map for further analysis. The sky map used equatorial sky coordinates with its origin at the center of the moon. To assure equal area bins throughout the sky, the axes were $\Delta\delta = (\delta_{Event} - \delta_{Moon})$ for the ordinate and $\Delta\alpha = (\alpha_{Event} - \alpha_{Moon}) \times \cos(\delta_{Moon})$ for the abscissa. Events were put into $0.1° \times 0.1°$ bins in the sky map.

3.2 Background
The method of generating background events has been described previously. [20, 19] In this method, the background is generated from the data itself under the assumptions that the detector efficiency in local coordinates is constant over 2-hour periods (although the overall event rate may

change) and that the distribution of background events at each declination follows the shape of the detected events. The second assumption breaks down in declination bands that include the moon. The method leads to an underestimate of the size of the background and, consequently, an underestimate of the observed event deficit caused by the moon of ~5%.[21]

3.3 Event Map

Figure 6 shows the significance of the event deficit in the vicinity of the moon with and without the correction for the systematic pointing error. In these plots, the significance is calculated for each bin using the events in the $2.1° \times 2.1°$ area surrounding the bin. This bin size is appropriate for the expected angular resolution of Milagrito for events with $N_{Fit} > 30$. [13] The observed shadow has a significance of 10.2σ. As expected, the correction appears to align the shadow in δ but the shadow is offset in α due to the geomagnetic field.

The width of the deficit in δ can be used to extract the angular resolution of Milagrito. This is done by subtracting the background sky map from the corrected data sky map and projecting the result onto the two axes. The results are given in Table 2. The angular resolution is poorest for events with a low value of N_{Fit}, but does not improve for events with the largest value of N_{Fit}. This is because the shower core is not well determined especially when the core is outside the pond.

Quantity	N_{Fit} Region	RMS Width
α	30-70	1.09° ±0.22°
α	70-120	0.72° ±0.15°
α	>120	0.78° ±0.19°
α	30-228	0.90° ±0.11°
δ	30-70	1.09° ±0.25°
δ	70-120	0.65° ±0.15°
δ	>120	0.79° ±0.20°
δ	30-228	0.90° ±0.13°

Table 2: Widths (rms) from Gaussian fits to projections of the corrected background-subtracted event deficit from the moon.

The geomagnetic deflection should broaden the shadow, primarily in the α projection, but this is not apparent in the results. The angular resolution of Milagrito for cosmic ray events as given in Table 2 is in good agreement with previous estimates [13] and with expectations from the simulations. Strictly speaking, the angular size of the moon should be deconvolved from the measured widths to derive the instrumental response, but this has a negligible effect on the results.

3.4 Maximum Likelihood Analysis

A maximum likelihood analysis adapted from Kinnison [22] is used to derive accurate information from the data. Each (corrected) event is represented by a vector: $\bar{x}_i = (\boldsymbol{a}_i, \boldsymbol{d}_i)$, and we assume that there are two populations of events, background and "signal." $M(\bar{x}_i)$ is the normalized probability distribution of the signal (moon deficit) events and $B(\bar{x}_i)$ is the normalized probability

distribution of the background events. There are N total events, of which n are signal and (N-n) are background. Then the partial probability density of the ith event is given by: with the requirement that

$$\sum_{i=1}^{N} P(\vec{x}_i) = 1.$$

The likelihood function is then given by:

$$L(n, \vec{x}) = \prod_{i=1}^{N} P(\vec{x}_i).$$

It is more practical to use the likelihood ratio, which is ratio of the likelihood function for the hypothesis that there are both signal and background events to the likelihood function for the null (no signal) hypothesis. The likelihood ratio is given by:

$$R(n, \vec{x}_i) = \frac{L(n, \vec{x}_i)}{L(0, \vec{x}_i)} = \prod_{i=1}^{N} \{\frac{n}{N}(\frac{M}{B} - 1) + 1\}.$$

For a search for a deficit, the number of events, n, is expected to be negative. For ease in calculations, the logarithm of the likelihood ratio function is used. The function ($2 \ln R$) should be distributed like a χ^2 distribution with the appropriate number of degrees of freedom [Eadie] (for the present analysis there are 3 degrees are freedom: α, δ, and n). This property facilitates the calculation of the statistical significance of the result.

The maximum likelihood method is well suited to a binned analysis. The probability distribution functions can be calculated for each bin and stored in an array. The events are also stored in binned event maps. $M(\vec{x}_i)$, the probability distribution function for events from the moon, is obtained from the corrected simulated shadow (the bottom plot in Figure 2) normalized to 1 over the entire region. $B(\vec{x}_i)$, the probability distribution function for background events, is obtained from the normalized background sky map.

4. Results

4.1 Position and depth of the shadow

Figure 7 shows the result of the maximum likelihood analysis of the data: Figure 7a (7b) shows the significance of the event deficit (number of events in the deficit) as a function of the assumed position of the center of the deficit. The results of the maximum likelihood fits to the data and the simulated data are given in Table 3.

Input	α	δ	Deficit
Data	-0.34° ± 0.14°	-0.02° ± 0.12°	17834 ± 1785 events
Simulation	-0.25° ± 0.13°	-0.09° ± 0.15°	22132 ± 2090 events

Table 3. The best-fit position and number of events from the maximum likelihood fit to the moon shadow.

The location of the center of the deficit for the data agrees within errors with the expected location from the simulation. The results in Table 3 indicate that the absolute pointing error for Milagrito is no larger than ~0.1°, after correcting for the effects of the late light. The amount of the deficit is somewhat smaller than expected, even after allowing for the effect of the underestimated background, discussed above. The discrepancy is concentrated in events with small values of N_{Fit}, and is probably due to the fact that the simulation does not correctly model all aspects of the late light, especially the scattering of light in the water.

4.2 Error in the Energy Scale

The agreement between the observed and expected position of the center of the shadow in α, the direction in which the shadow is deflected by the geomagnetic field, can be used to limit any difference between the energy scales in the simulation and the data. Milagrito responds to air-shower particles at ground level, not to the energy of the primary cosmic ray. The connection between the ground-level particles and the primary energy is made only indirectly in the Monte Carlo program that simulates the air shower. However, the deflection of the primary cosmic rays and the position of the detected shadow of the moon directly measure the magnetic rigidity of the primary cosmic rays. Thus the position of the shadow of the moon allows a direct comparison between the scale of the magnetic rigidity of detected particles in Milagrito and in the simulation. Figure 8 compares the displacement of the shadow as the energy scale in the simulation is varied with the measured position of the shadow. This implies that the ratio of the energy scale for detected events to the energy scale of simulated events is bounded (~1 standard deviation) by:

$$0.5 < \frac{\langle E_{obs} \rangle}{\langle E_{sim} \rangle} < 2.1.$$

While this is not a very restrictive bound, it is the first direct ground-based measurement of primary cosmic-ray energies. This technique will lead to improved bounds using Milagro [21], which has better angular resolution, no appreciable systematic pointing error, and larger statistics.

4.3 Cosmic Antiprotons

As discussed in the Introduction, high-energy cosmic antiprotons would produce a moon shadow displaced by the geomagnetic field the direction opposite to the displacement of the cosmic ray shadow. The search for an antiproton shadow was made by extending the likelihood function to

include a third probability distribution function and maximizing the likelihood as a function of the number of events in the cosmic ray shadow, n_{cr}, and the number of events in the antiproton shadow, $n_{\bar{p}}$. The antiproton shadow is simulated assuming that the cosmic antiprotons have the same spectral shape as the protons: no anti-Helium or other anti-nuclei were included in the simulation. To reduce the number of degrees of freedom, the antiproton shadow was constrained to be centered at the same declination as the cosmic-ray shadow and to have $\alpha_{\bar{p}} = -1.15 \, \alpha_{matter}$, i.e. equal and opposite to the best position of the shadow from the cosmic protons. The results of this maximum likelihood fit are shown in Figure 9. The maximum of the likelihood ratio occurs in the unphysical region (a small excess of events in the antiproton shadow). The 95% confidence upper limit for the number of antiproton events blocked by the moon using only the physical region is:

$$|n_{\bar{p}}| < 2400 \text{ (95\% CL).}$$

Comparing this with observed number of cosmic-ray events blocked by the moon (17834), we find:

$$n_{\bar{p}} / n_{cr} < 0.13 \text{ (95\% CL),}$$

or

$$n_{\bar{p}} / n_{p} < 0.17 \text{ (95\% CL).}$$

The median proton (and antiproton) energy for these results is ~2.4 TeV. The maximum likelihood technique has been checked by adding a small antiproton shadow in the simulation and extracting the expected number of antiproton events.

This result is more restrictive than the upper limit on cosmic antiprotons derived using data from the Tibet array [12]. This result is also more restrictive than the upper limit on cosmic antiprotons, $n_{\bar{p}} / n_{p} < 0.22$ (84% CL) around 10 TeV [23], obtained from the sun shadow observed by the Tibet array.

4.4 Shadow of the Sun

The sun should also cast a shadow in cosmic rays. However, in addition to the displacement of the sun shadow from the geomagnetic field, the sun's magnetic field may also displace the observed shadow. The heliomagnetic field is known to vary strongly with time, and is not always well understood. Consequently, the study of the sun shadow was done without taking the heliomagnetic field into account. The Tibet group has reported that the location of the sun shadow observed with ~8-TeV cosmic rays varies year-to-year and is correlated with the solar and interplanetary magnetic fields. [24] The shadows observed in 1996 and 1997 were observed to be at the undeflected position of the sun.

The analysis of the sun shadow was similar to the analysis reported in section 3.3. Figure 10 shows the significance of the event deficit in the vicinity of the sun with and without the correction for the systematic pointing error: this is comparable to Figure 6. The position of the center of the deficit for the corrected data, which has a significance of 10.1σ, is

$$\alpha = -0.29° \pm 0.17°, \delta = 0.00° \pm 0.17°.$$

This is consistent with the expected displacement of the shadow ($\alpha = -0.19° \pm 0.19°$) in the absence of a heliomagnetic field, and serves as an independent check of the systematic pointing error.

5. Discussion

The cosmic-ray shadows of the moon and the sun have been seen with high significance with data from Milagrito. A study of the measured center of the shadow yields the following results:

1. Agreement between the simulation and data on the size and direction of the systematic pointing error caused by late light in Milagrito. After correcting this systematic error, the absolute pointing error is less than 0.1°.

2. The angular resolution of Milagrito improves as the number of PMTs used in the shower fit increases. The overall angular resolution is 0.90° rms.

3. The first direct ground-based measure of the energy of cosmic rays, which implies agreement between the simulated and observed energy scales to within a factor of 2.

4. An upper limit, $n_{\bar{p}}/n_p < 0.17$ (95% CL), on the flux of high-energy (~2.5 TeV) cosmic antiprotons. This is the best limit in this energy regime.

5. The solar magnetic field did not significantly displace the shadow during 1997-8.

REFERENCES
[1] Clark, G. W., Phys. Rev. **108**, 450 (1957).
[2] Lloyd-Evans, J., *Proceedings of the XIX International Cosmic Ray Conference*, La Jolla, CA, **2**, 173 (1985).
[3] Linsley, J., *Proceedings of the XIX International Cosmic Ray Conference*, La Jolla, CA, **3**, 465 (1985).
[4] Alexandreas, D. E., *et al.* Phys. Rev. D **43**, 1743 (1991).
[5] Amenomori, M. *et at.*, Phys. Rev. D **47**, 2675 (1993); Amenomori, M., *et al.*, Ap. J. **415**, L147 (1993).
[6] Borione, A., *et al*, Phys. Rev. D **49**, 1171 (1994).
[7] Aglietta, M., *et al.*, Astroparticle Phys. **3**, 1 (1995).
[8] Krawcznski, H., *et al*, Nucl. Instru. and Meth. A **383**, 431 (1996).
[9] Amenomori, M., *et al.*, Ap. J. **541**, 1051 (2000).
[10] Urban, M., P. Fleury, R. Lestienne, F. Plouin, Nucl. Phys. B (Proc. Suppl.) **14B**, 223 (1990); Urban, M., P. Fleury, E. Paré, F. Plouin, *Toward a Major Atmospheric Detector for TeV Astroparticle Physics*, P Fleury, G. Vacanti (Eds.), 152 (1992).
[11] Pomarède, D., *et al.*, Astroparticle Phys. **14**, 287 (2001).
[12] Chantell, M. *et al.*, Nature, **367,** 25 (1994).
[13] Atkins, R., *et al.*, Nucl. Instrum. Meth. Phys. Res. **449A**, 478 (2000).

[14] Heck, D., *et al.*, "CORSIKA: A Monte Carlo Code to Simulate Extensive Air Showers" Forschungzentrum Karlsruhe, Wissenschaftliche Berichte FZKA 6019 (1998); Klages, H. O., *et al.*, Nucl.Phys. B (Proc. Suppl.) **52**, 92 (1997).

[15] Asakimori, K., *et al*., Ap. J. **502**, 278 (1998).

[16] Wiebel-Sooth, K., P. L. Biermann & H. Meyer, Astron. Astrophys. **330**, 389 (1998).

[17] Nelson, W. R., *et al*., SLAC Report 265 (1985).

[18] National Geophysical Data Center, http://www.ngdc.noaa.gov/seg/potfld/geomag.shtml (2001).

[19] Atkins, R., *et al.*, Ap. J. **525**, L25 (1999); Wang, K., *et al*., to be published in Astrophysical Journal (2001).

[20] Alexandreas, D. E., *et al.*, Ap. J. **383**, L53 (1991); Alexandreas, D. E., *et al.*, Nucl. Instrum. Meth. Phys. Res. **A328**, 570 (1993).

[21] Samuelson, F. *et al.*, submitted to XXVII International Cosmic Ray Conference, Hamburg, Germany (2001).

[22] Kinnison, W. W., *et al.*, Phys. Rev. **D25**, 2846 (1982).

[23] Amenomori, M., *et al.*, *Proceedings of the XXIV International Cosmic Ray Conference*, Rome, Italy, **3**, 84 (1995).

[24] Amenomori, M., *et al.*, Ap. J. **541**, 1051 (2000).
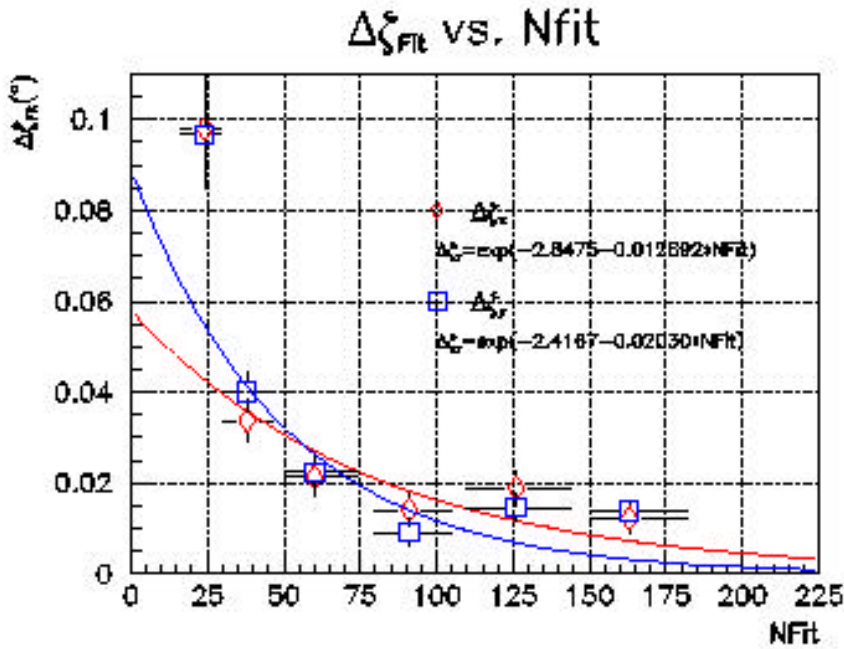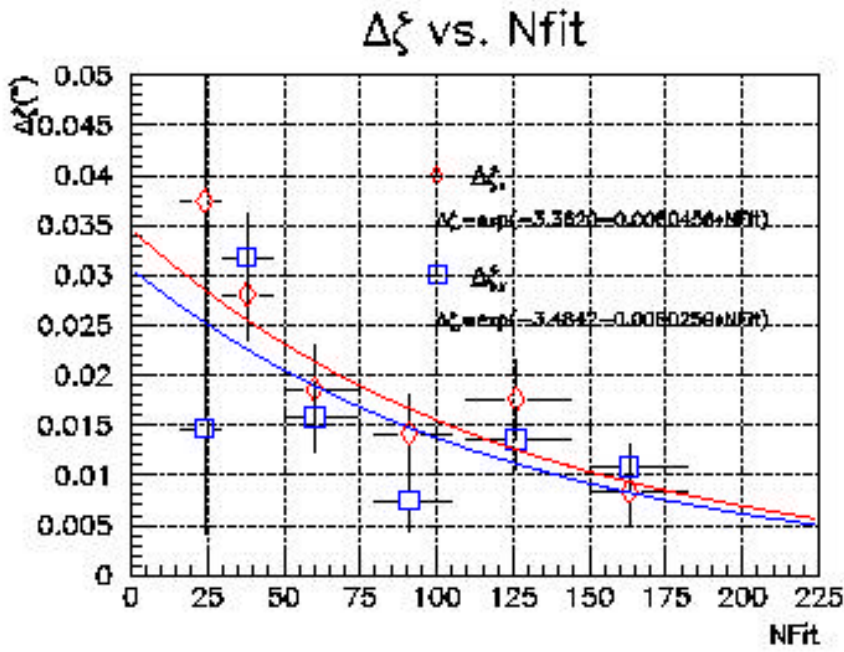
Figure 1: The dependence of the systematic pointing error on N_{Fit}, the number of PMTs participating in the event fit. The top plot shows the result of fitting $\Delta\zeta_{x,y}$ vs. $\zeta_{x,y}^{Thrown}$, and the bottom plot shows the result of fitting $\Delta\zeta_{x,y}$ vs. $\zeta_{x,y}^{Fit}$.
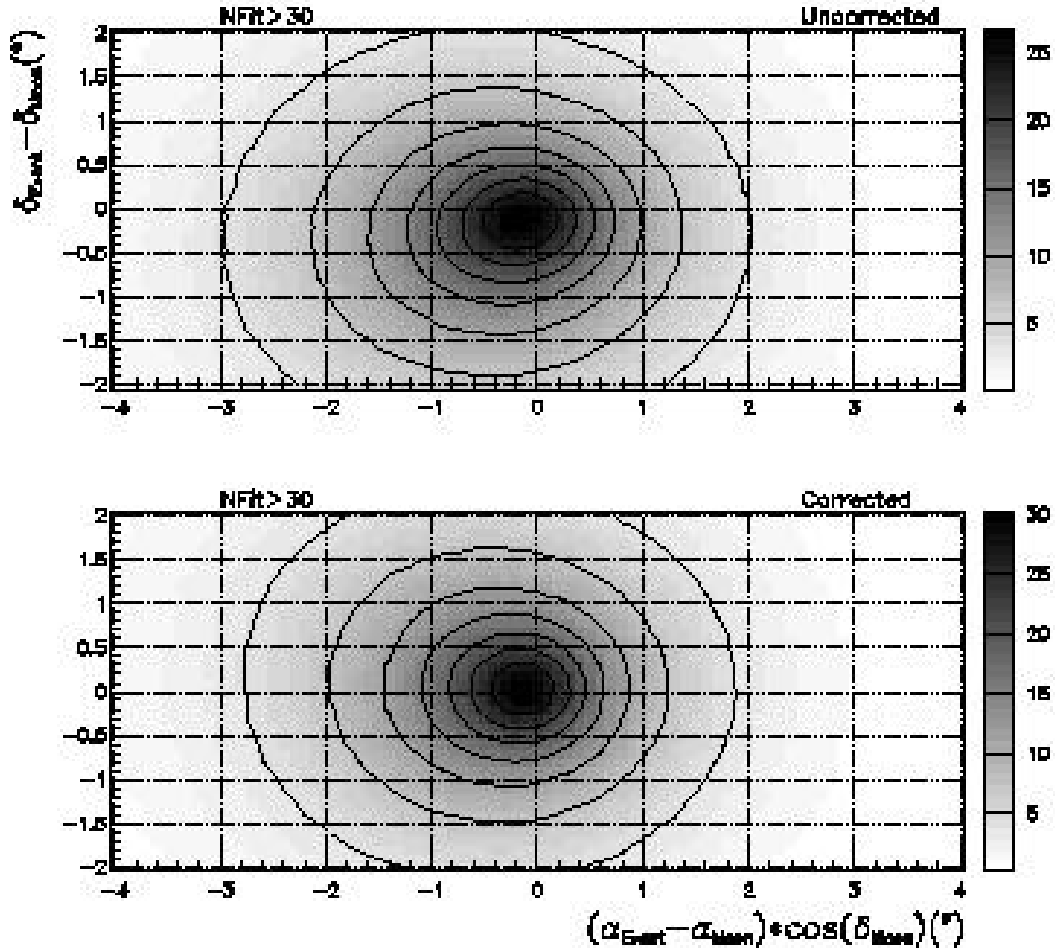
Figure 2: The simulated shadow of the moon for Milagrito. The top plot is uncorrected, and the bottom plot is corrected for the systematic pointing error, as described in the text. This is the distribution of only those simulated events that would be blocked by the moon. The events are plotted vs. the difference in declination (δ) and right ascension (α) times $\cos(\delta_{Moon})$ and the actual position of the center of the moon. The grey-scale, given on the right of each plot, indicates the number of events in each $0.1° \times 0.1°$ bin.

13
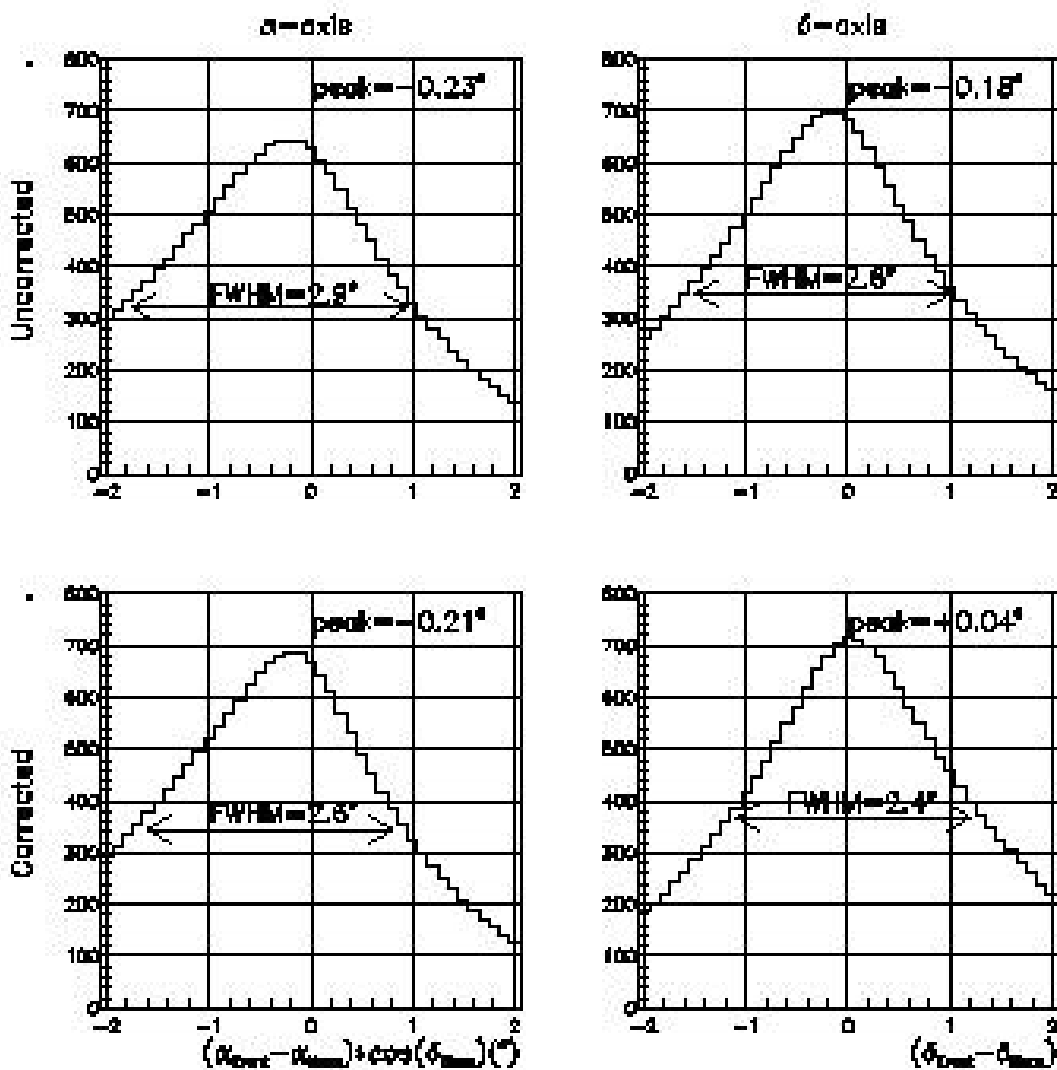
Figure 3: Projections of the simulated shadows from Figure 2 onto the declination (δ) and right ascension (α) times $\cos(\delta_{Moon})$ axes. The top two plots are for the uncorrected moon shadow and the bottom two plots are corrected for the systematic pointing error.

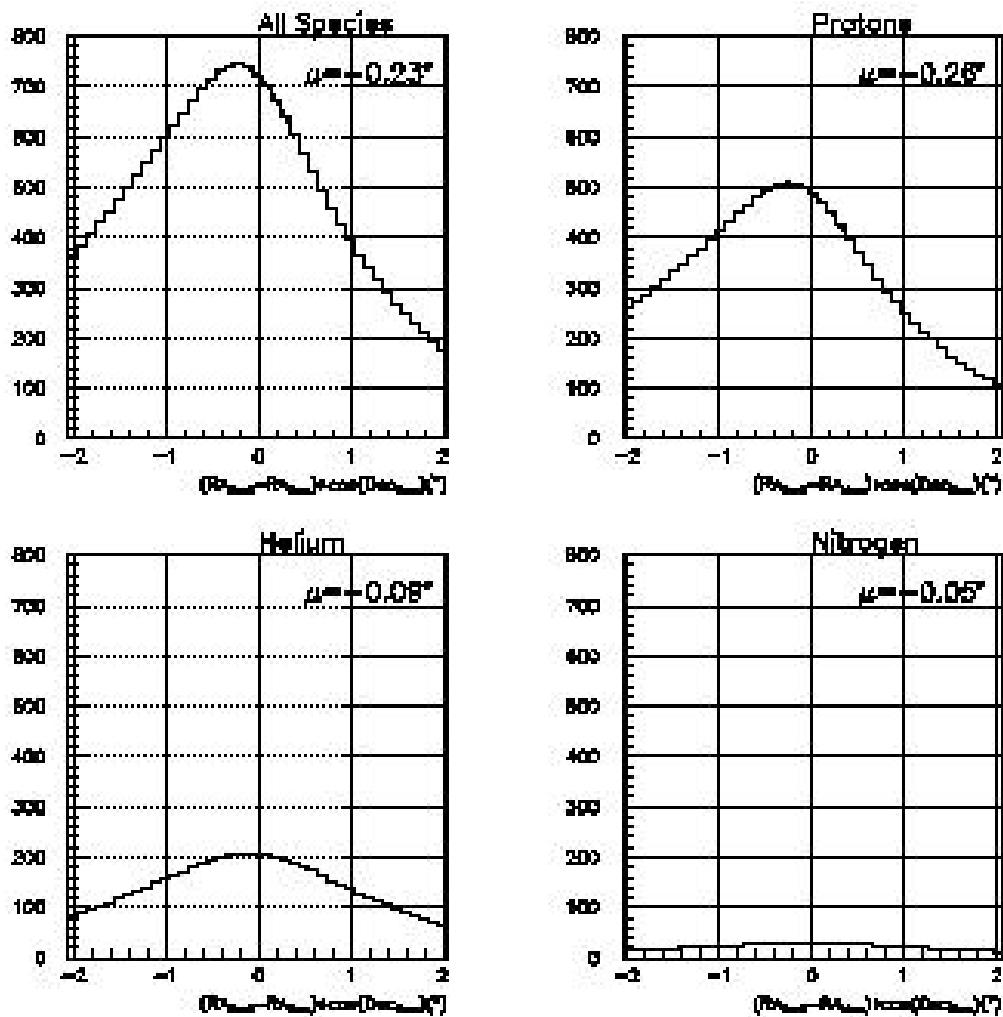Figure 4: The projection of the simulated moon shadow onto the right ascension (α) times $\cos(\delta_{Moon})$ axis for protons, helium, nitrogen, and the sum of all species. The shadow shown has not been corrected for the systematic pointing error.
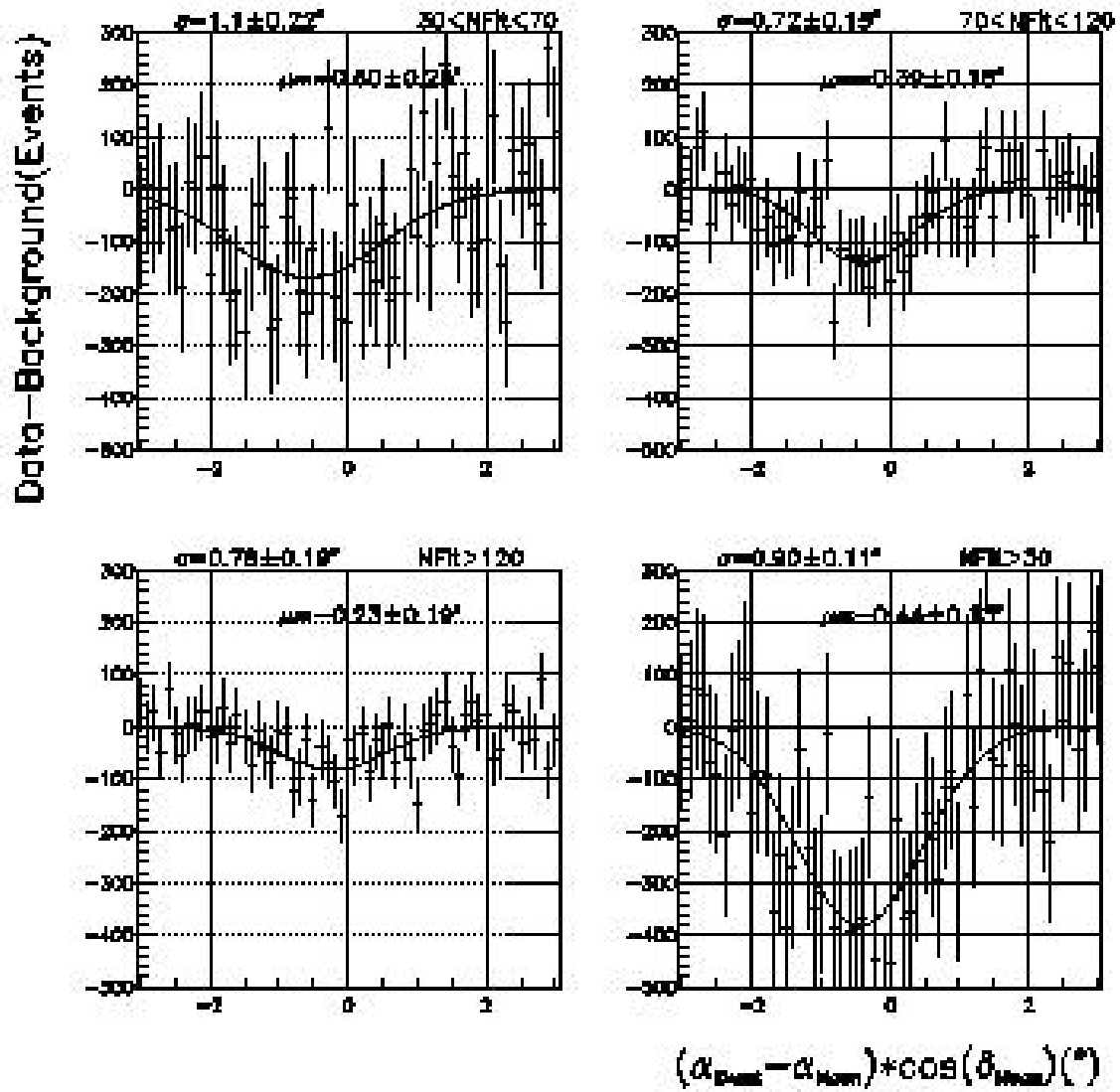
Figure 5: Projection of the data onto the α axis of a 2° band in δ of the moon shadow for different bands of N_{Fit}. The lines indicate a Gaussian fit to the deficit.
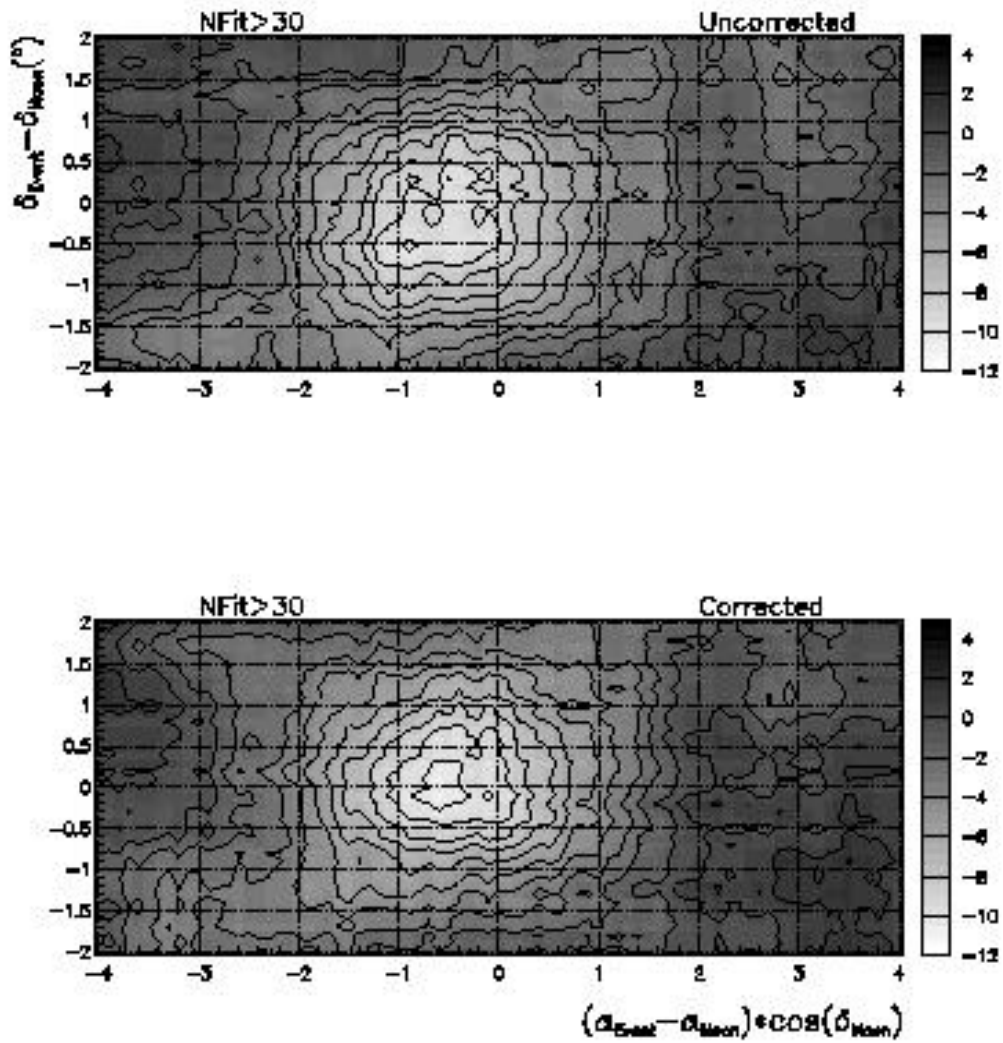
Figure 6: The significance of the moon shadow from the event map. The lower (upper) plot shows the data before (after) correction for the systematic pointing error. The grey scale on the left shows the significance in standard deviations.
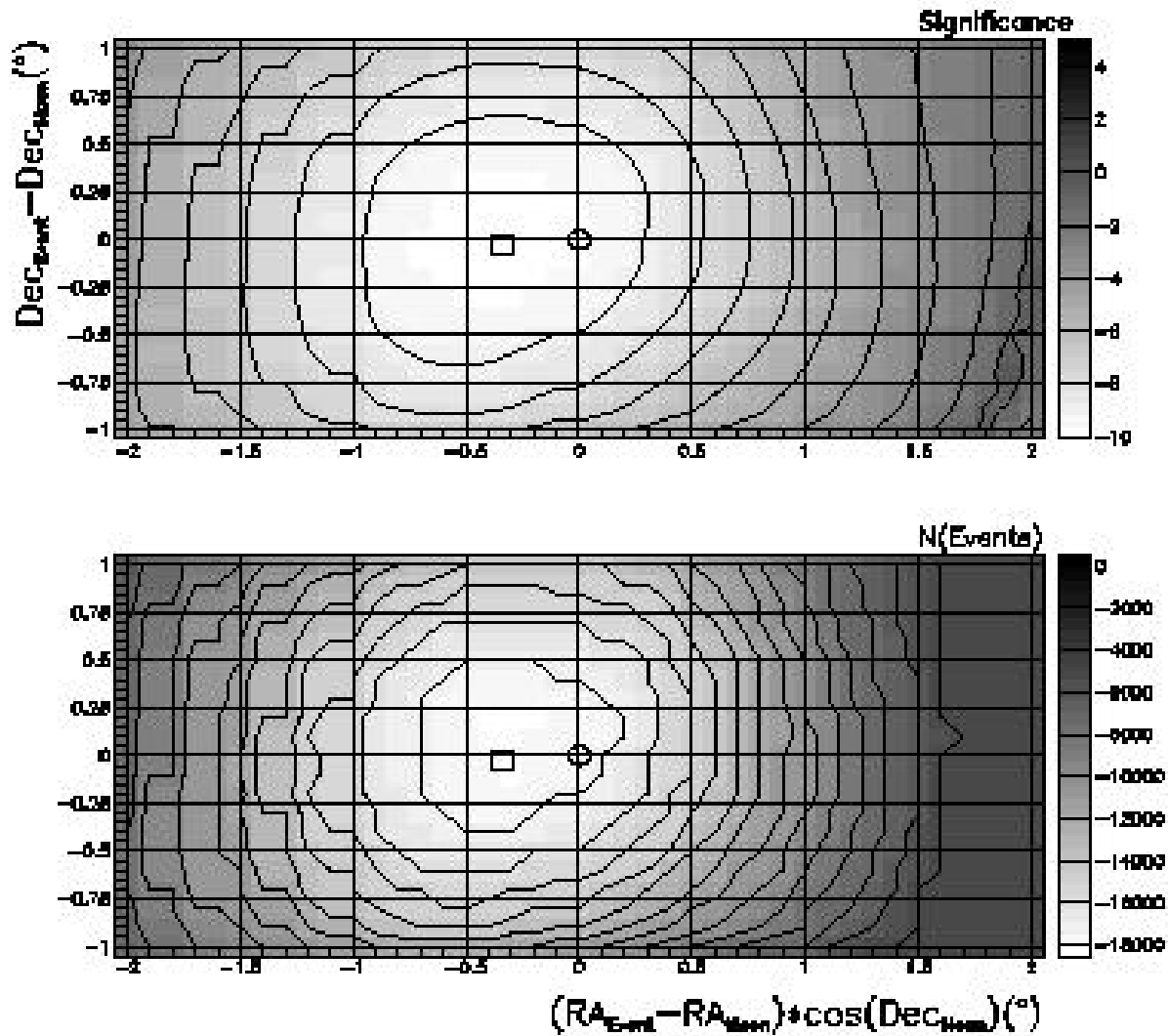
Figure 7: The result of the maximum likelihood fit to the moon shadow shown as a function of the position of the center of the event deficit. The top plot shows the significance and the bottom plot shows the number of events in the shadow. In each plot, the small square shows the position of the maximum of the likelihood function and the small circle shows the undeflected position of the moon.
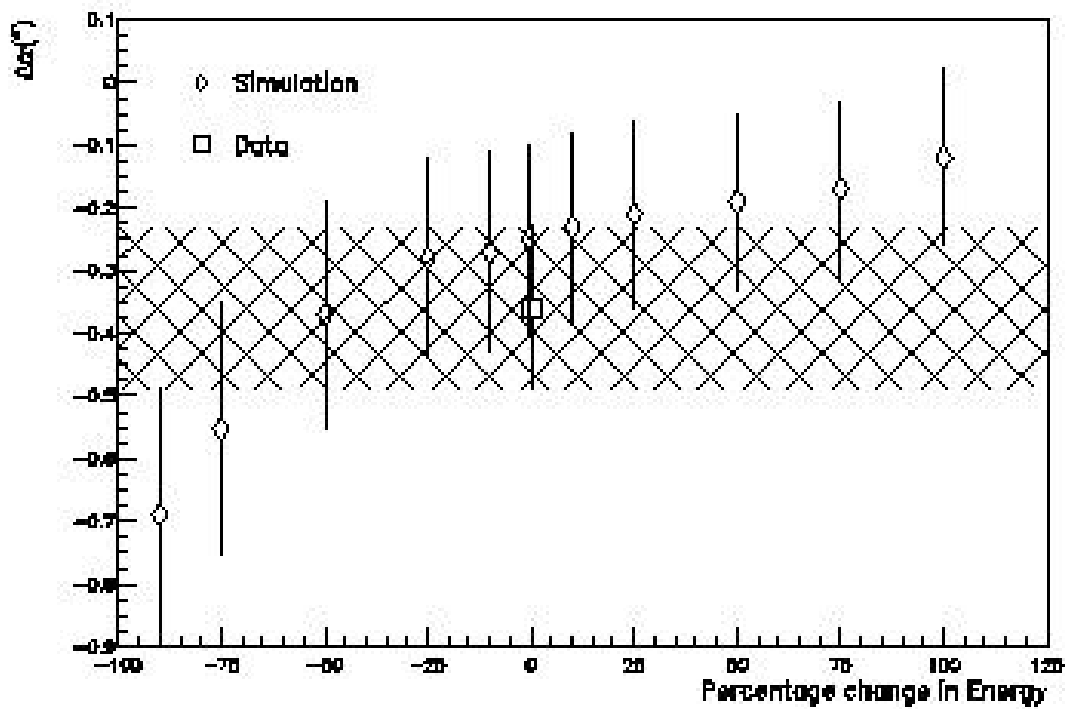
Figure 8: The offset in the moon shadow in right ascension. The points for the simulation indicate the offset that results in rescaling the primary energy (without changing the shower at ground level). The cross-hatched region is the 1σ region of the offset from the data.
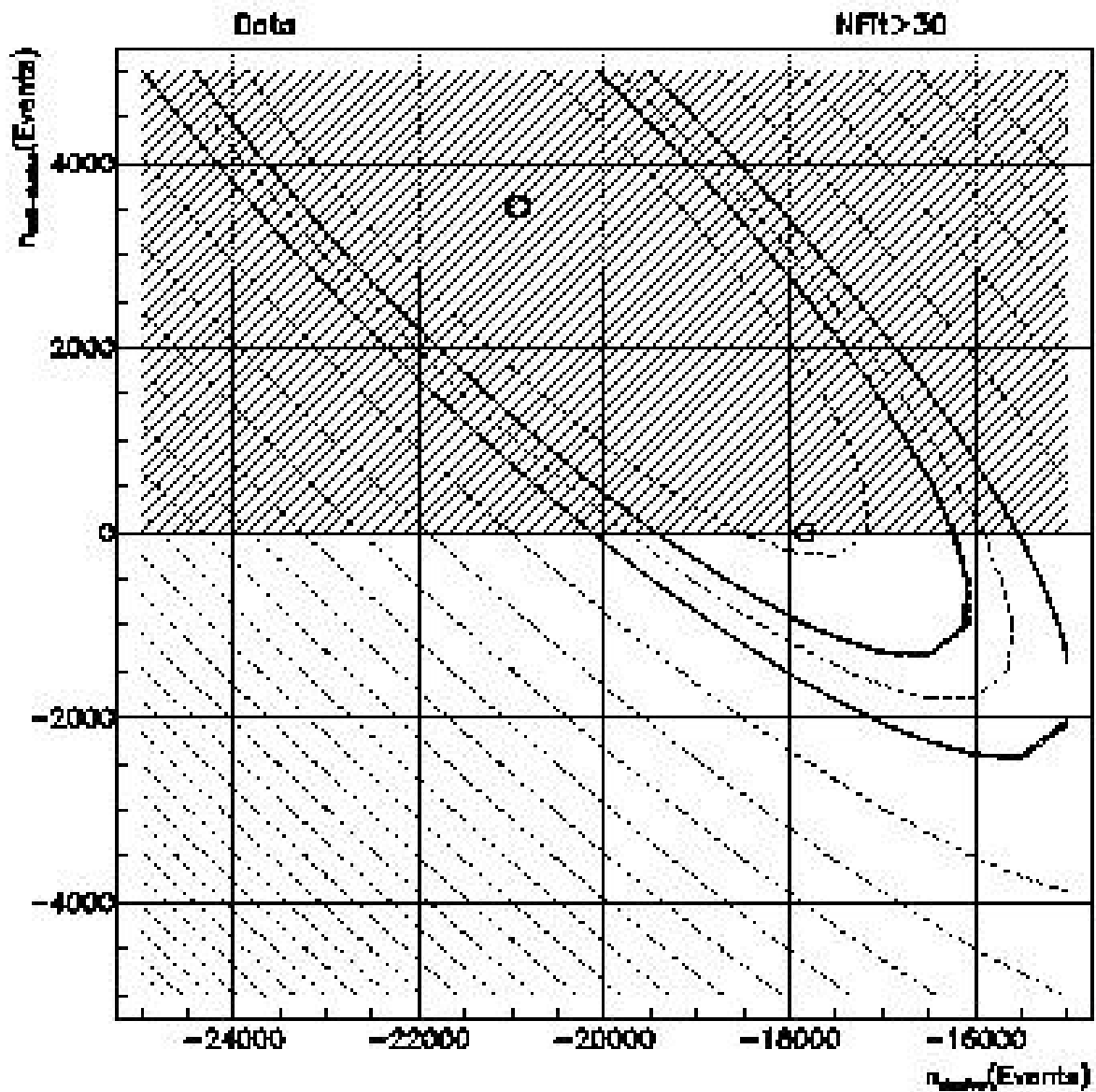
Figure 9: A contour plot of the logarithm of the likelihood vs. the number of cosmic ray and antiproton events shadowed by the moon. The dark circle is the overall maximum of the likelihood function and the lighter circle is the maximum in the physical region. Each contour represents 1σ in significance. The darker contours are the 95% confidence level for the overall and physical maxima.

20